Wind and Structures, *Vol. 40, No. 2 (2025) 93-105*
https://doi.org/10.12989/was.2025.40.2.093

Coupled flutter mechanism of flexible suspended pedestrian bridges

Sanghyeon Lee[1], Youchan Hwang*[2] and Ho-Kyung Kim[1,2,3]

[1]*Department of Civil and Environmental Engineering, Seoul National University, Seoul, 08826, Republic of Korea*
[2]*Floating Infrastructure Research Center, Seoul National University, Seoul, 08826, Republic of Korea*
[3]*Institute of Construction and Environmental Engineering, Seoul National University, Seoul, 08826, Republic of Korea*

(*Received September 3, 2024, Revised December 16, 2024, Accepted January 29, 2025*)

Abstract. Flexible suspended pedestrian bridge (FSPB) is a distinctive structure with a taut catenary shape in which separated deck modules are supported by suspension cables. FSPBs are characterized by high flexibility and large deformation arcs due to their low structural stiffness and damping, exhibiting significant aeroelastic interactions between modes. This study focused on flutter, an aeroelastic instability issue, in FSPBs. Wind tunnel tests and numerical analyses were conducted on two deck designs: open grating (OG), which minimizes air resistance, and solid deck (SD), which fully blocks the deck grating. Results showed that SD exhibited relatively vulnerable aeroelastic behavior, while the OG demonstrated greater stability against flutter. Numerical analysis explored the mode coupling of the entire bridge, examining the influence of lateral modes and degrees of freedom (DOF) on the onset of coupled flutter in the SD. The applicability of a two-dimensional (2-D) wind tunnel test setup was also examined. Additionally, the study identified the developing mechanism of torsional-vertical coupled flutter and key parameters influencing critical modes using 2-D wind tunnel tests and time-domain flutter analysis.

Keywords: aeroelastic flutter analysis; coupled flutter; flexible suspended pedestrian bridge (FSPB); wind tunnel test

1. Introduction

A flexible suspended pedestrian bridge (FSPB) is a structural system where segmented deck modules, composed of slender frames and protective wires, are supported by multiple cables. FSPBs have a taut catenary shape along their suspension cables due to the minor contribution of segmented decks to structural stiffness. These cables cannot resist in-plane or out-of-plane bending moments, leading to significant sag and deformation. Compared to long-span suspension road bridges, FSPBs have a significantly higher aspect ratio, defined as the span-to-width ratio, which reflects their flexibility. Typically, FSPBs are around 2 m wide, with span lengths ranging from 150 m to over 700 m. For instance, the 516 Arouca Bridge, one of the world's longest FSPBs built in 2020, has an aspect ratio of 246. In contrast, the 1915 Çanakkale Bridge, one of the world's longest suspension road bridges, has an aspect ratio of only 45. The lower stiffness and damping of FSPBs make them more vulnerable to substantial vibrations caused by dynamic loads than conventional road bridges (Jiménez-Alonso *et al*. 2016, Tubino 2018, Venuti *et al*. 2016). Moreover, FSPBs are intentionally designed to provide a certain vibration level for the pedestrians' enthusiasm. In Korea, a specialized design guideline (MOLIT 2021) was recently developed to ensure the safety and functionality of FSPBs.

These FSPBs are mainly installed on cliffs or canyons, frequently exposing them to severe wind conditions. The distinctive structural characteristics of FSPBs can lead to aerodynamic instability issues that are not typically encountered in conventional road bridges (Ma *et al.* 2020). Previous studies have focused on the flutter responses of FSPBs distinguishing them from long-span road bridges, and investigated methods to improve aerodynamic stability. Rizzo *et al.* (2018) conducted wind tunnel tests and flutter analysis, considering experimental measurement errors, to evaluate the flutter stability of pedestrian suspension bridges. Li and Li (2020) evaluated the correlation that the presence of pedestrians exerts on the flutter derivatives of a suspended footbridge. Guan *et al.* (2022), and Liu *et al.* (2020) experimentally investigated the effectiveness of aerodynamic vibration control methods such as decorative wind chimes, twin decks, fairing, and wind-restraint plates on the flutter stability of a suspended footbridge.

The methodologies used in previous studies to evaluate vibrations with two-dimensional (2-D) wind tunnels are similar to those for assessing the wind stability of conventional road bridges. However, since the governing torsional modes of FSPBs can induce significant lateral motion along the span due to the structure's low lateral stiffness, raising uncertainty about the lateral degrees of freedom (DOF) on the flutter stability of FSPBs. Thus, it is necessary to explore whether the traditional 2-D wind tunnel test setups are suitable for assessing the wind stability of FSPB. Additionally, understanding the flutter-developing mechanism is crucial to fundamentally prevent flutter instability issues and to identify the triggers that cause distinct responses in FSPGs compared to long-span road bridges, requiring detailed investigations from various perspectives.

This study primarily examined the applicability of the 2-D wind tunnel test setups and the flutter-developing

*Corresponding author, Ph.D.
E-mail: lum4u2526@snu.ac.kr

Copyright © 2025 Techno-Press, Ltd.

ISSN: 1226-6116 (Print), 1598-6225 (Online)

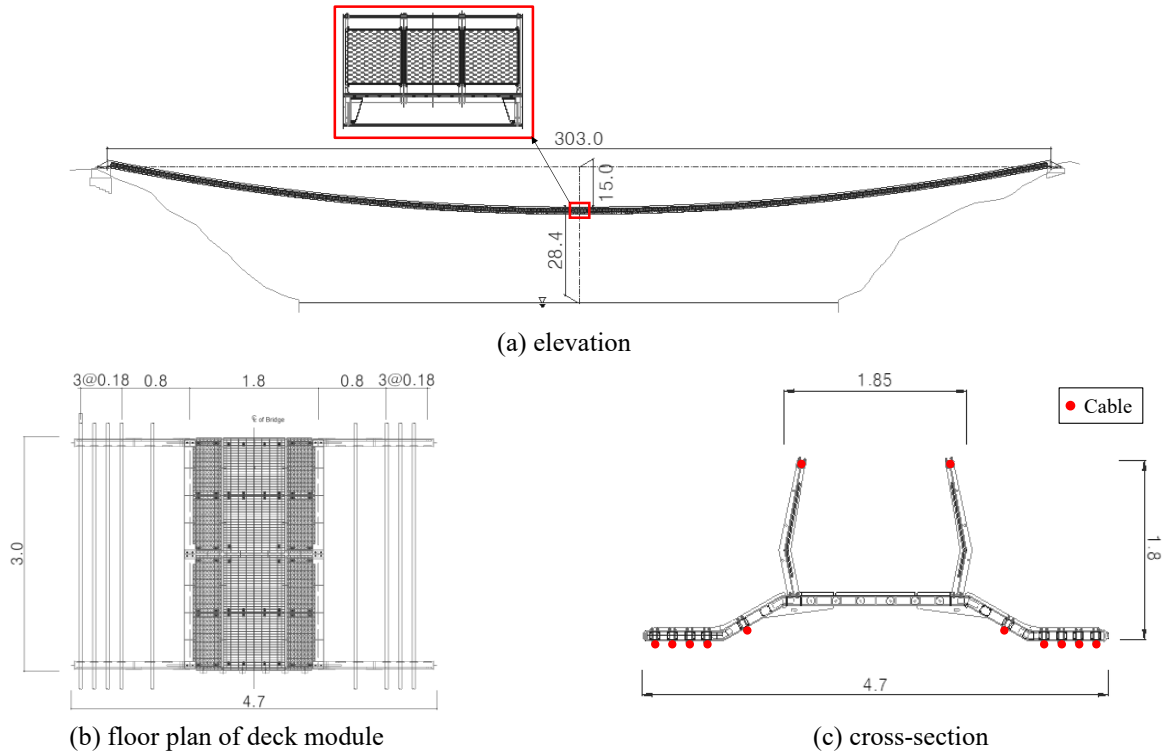

(a) elevation

(b) floor plan of deck module

(c) cross-section

Fig. 1 Prototype bridge (unit: m)

mechanisms in FSPBs. Wind tunnel tests and numerical analyses were conducted, considering two comparative cross-sectional designs to ensure aerodynamic stability. The contribution of lateral modes and lateral DOF on the flutter development and behavior was numerically evaluated using a three-dimensional finite element model of the entire bridge system. A state-of-the-art approach, a time-domain aeroelastic analysis based on a Fourier Series Approximation (FSA) of frequency-dependent self-excited forces (Park *et al*. 2014), was adopted to investigate the aeroelastic behavior and identify key parameters contributing to flutter instability. The findings from aeroelastic analysis validated the applicability of the 2-D wind tunnel test setups for vertical and torsional DOF while restraining the lateral motion in FSPBs. Coupled flutter behavior was successfully demonstrated in both wind tunnel tests and numerical analyses. From the contribution of the aeroelastic self-excited forces and damping based on time-domain analysis, it was confirmed that the flutter-development mechanism arises from the coupling effect of vertical-torsional DOFs. Additionally, both unstable aeroelastic parameters and a low frequency ratio (FR) between the two critical modes were discussed as the key factors contributing to flutter instability at low wind speeds.

2. Prototype bridge

2.1 Structural dimensions

The Daewangam Suspension Footbridge, opened in 2021 in South Korea, served as the prototype bridge for this study. Fig. 1 illustrates the configuration and cross-section of the prototype bridge. The structure consists of 101 segmented modules suspended by a series of cables with a span length of 303 m and a constant deck width of 1.85 m, resulting in an aspect ratio of 164.

During the design phase, it was necessary to carefully examine how the opening ratio of the deck grating influenced aerodynamic stability, considering both open grating (OG) and a solid deck (SD). The OG design minimizes air resistance by allowing undisturbed wind flow, while the SD design completely blocks wind flow by covering the grating with wood or tempered glass, which also applies if the grating becomes unexpectedly blocked by snow.

2.2 Aerodynamic and aeroelastic parameters

To assess the aerodynamic stability of the prototype bridge, aerodynamic and aeroelastic parameters were experimentally obtained through testing in an open-circuit wind tunnel at Seoul National University, South Korea. The test section of the wind tunnel had dimensions of 1 m in width, 1.5 m in height, and 6 m in length. The maximum wind speed was 23.0 m/s, and the turbulence intensity was lower than 0.5%. The geometric scale of the section model used was 1/12, resulting in a section model with dimensions of 0.154 m in width, 0.15 m in height, and 0.9 m in length. The main bodies of the section model were made of balsa wood. The handrails and deck gratings were manufactured to have an equivalent porosity (6.1 and 20.5 %, respectively) that was consistent with the prototype bridge. Fig. 2 shows the plane view of the OG and SD section models.

The flutter derivatives, denoted as H_i^*, A_i^*, and P_i^* (i = 1,

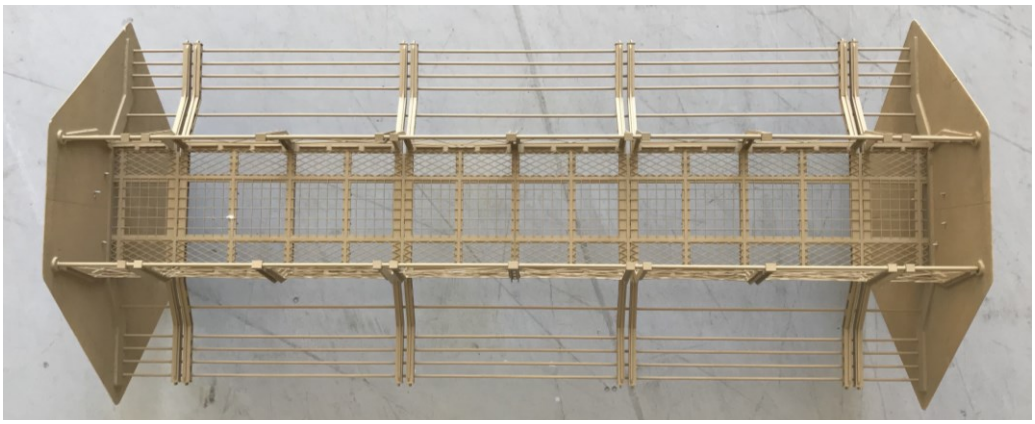

(a) OG

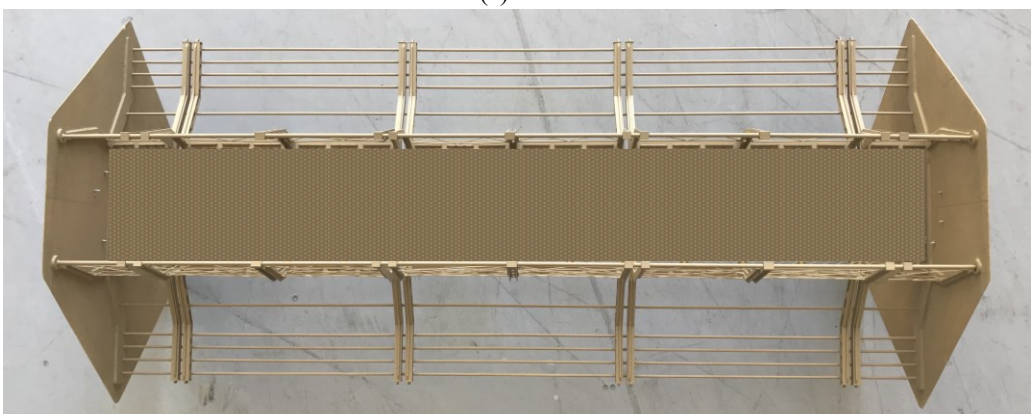

(b) SD

Fig. 2 Plane view of the section model

..., 6), were defined to calculate the self-excited forces per unit span of a bridge deck. These forces include the lift force L_{se}, pitching moment M_{se}, and drag force D_{se}, and their formulations are as follows (Sarkar *et al*. 1994).

$$L_{se} = \frac{1}{2}\rho U^2 B\left(KH_1^*\frac{\dot{h}}{U} + KH_2^*\frac{B\dot{\alpha}}{U} + K^2H_3^*\alpha + K^2H_4^*\frac{h}{B} + KH_5^*\frac{\dot{p}}{U} + K^2H_6^*\frac{p}{B}\right) \quad (1)$$

$$M_{se} = \frac{1}{2}\rho U^2 B^2\left(KA_1^*\frac{\dot{h}}{U} + KA_2^*\frac{B\dot{\alpha}}{U} + K^2A_3^*\alpha + K^2A_4^*\frac{h}{B} + KA_5^*\frac{\dot{p}}{U} + K^2A_6^*\frac{p}{B}\right) \quad (2)$$

$$D_{se} = \frac{1}{2}\rho U^2 B\left(KP_1^*\frac{\dot{p}}{U} + KP_2^*\frac{B\dot{\alpha}}{U} + K^2P_3^*\alpha + K^2P_4^*\frac{p}{B} + KP_5^*\frac{\dot{h}}{U} + K^2P_6^*\frac{h}{B}\right) \quad (3)$$

In formulations, h, α, and p are the vertical, torsional, and lateral displacements, respectively; the dot in the equations indicates the differentiation with respect to time; U is the mean wind velocity; ρ is air density; B is the bridge deck width; $K(=B\omega/U)$ is the reduced circular frequency; $\omega(=2\pi f)$ is the circular frequency; and, f is the vibration frequency in Hz. The signs of force and displacement were defined in such a way that positive values corresponded to upward movement, nose-up rotation, and windward movement of the deck in the vertical, rotational, and horizontal directions, respectively.

Flutter derivatives for both section models were obtained by conducting a pre-defined harmonic motion test at an attack angle of 0°. The amplitudes of the motion were maintained at 10 mm in the case of vertical motion and 0.6° for the torsional rotation. The excitation frequency was set to 1 Hz for both excitation modes. Flutter derivatives plotted against reduced velocity $(=U/(fB))$ for both sections are presented in Fig. 3. Due to equipment limitations, the harmonic motion tests were only conducted in the vertical and torsional directions. The flutter derivatives H_5^*, A_5^*, P_1^*, P_3^*, and P_5^* are related to the lateral motion and were estimated using quasi-steady theory (Strømmen 2010). The drag (C_D), lift (C_L), and moment (C_M) static coefficients at an attack angle of 0° and the slopes ($'$) between the attack angles of -1° and 1° for both section models are described in Table 1.

The aeroelastic instability of a bridge can be theoretically predicted from the magnitude and signs of the flutter derivatives. For both the OG and SD sections, single-mode torsional flutter was not expected because A_2^* had

Table 1 Static coefficients for both section models

Static coefficient	OG	SD
C_D	0.626	0.576
C_L	-0.268	-0.395
C_M	0.087	0.036
C_D'	-0.471	0.006
C_L'	0.733	5.029
C_M'	0.015	0.708

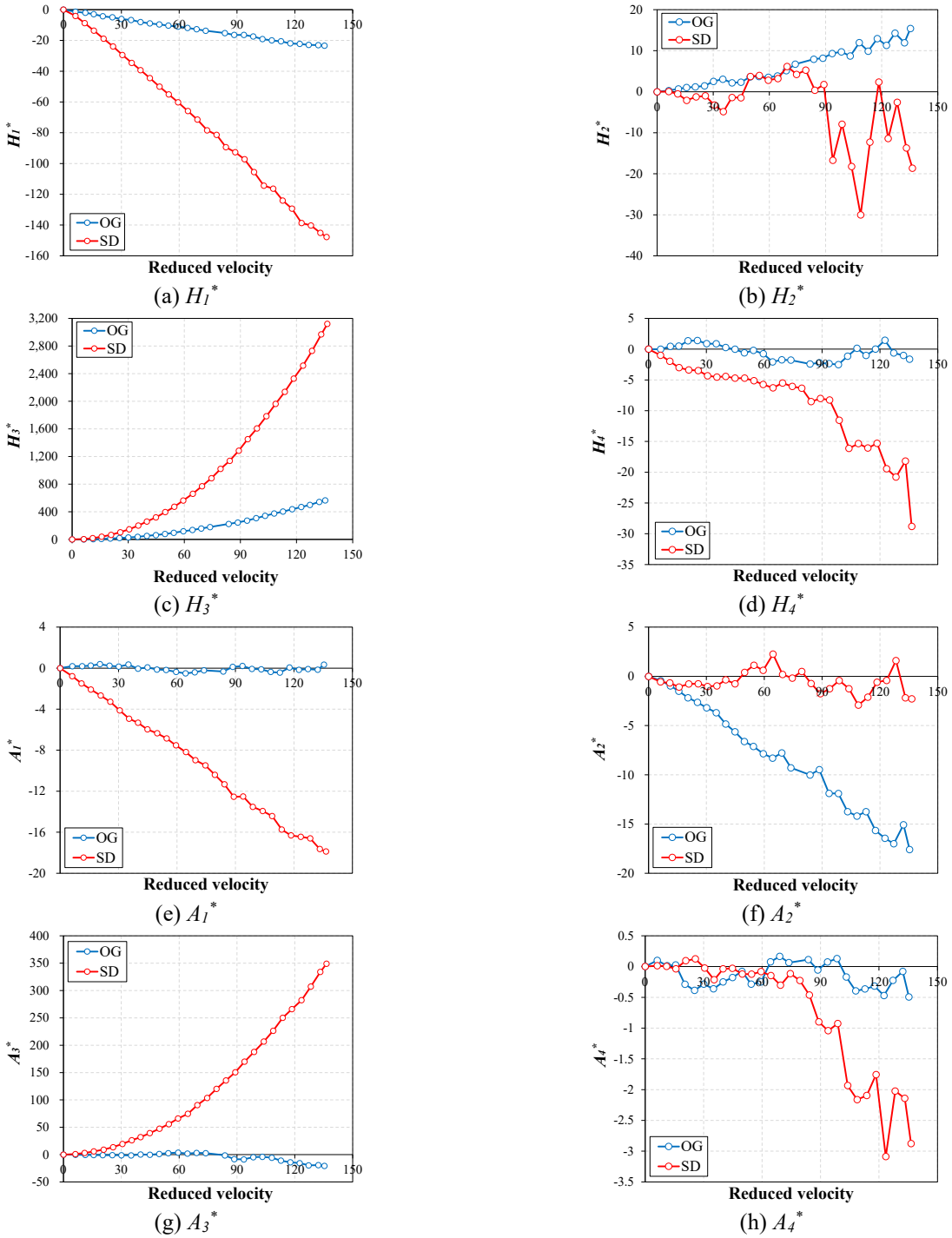

(a) H_1^* (b) H_2^*

(c) H_3^* (d) H_4^*

(e) A_1^* (f) A_2^*

(g) A_3^* (h) A_4^*

Fig. 3 Flutter derivatives for both section models

Table 2 Natural frequencies and mode shapes of the prototype bridge

Mode No.	Natural frequency (Hz)	Mode shape
1	0.147	L-S-1
2	0.283	V-A-1
3	0.293	L-A-1
4	0.358	V-S-1
5	0.440	L-S-2
6	0.446	T-A-1
7	0.471	T-S-1
8	0.475	V-S-2
9	0.571	V-A-2
10	0.588	L-A-2
11	0.626	T-A-2
12	0.720	V-S-3
13	0.733	L-S-3
14	0.779	T-S-2
15	0.857	V-A-3
16	0.879	L-A-3
17	0.971	T-S-3
18	1.001	V-S-4
19	1.026	L-S-4
20	1.142	V-A-4

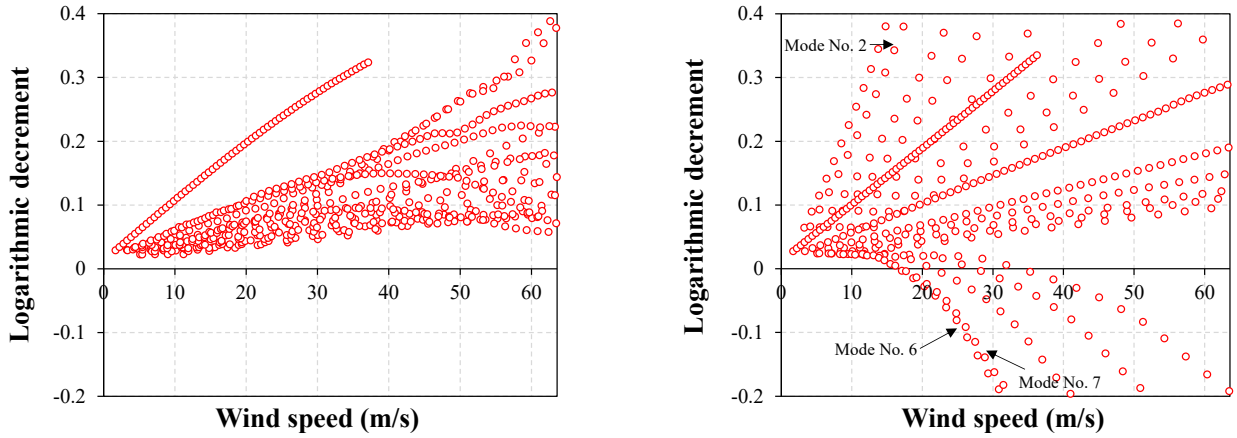

(a) OG (b) SD

Fig. 4 Changes in damping ratios obtained from CEVA

remained negative (Matsumoto *et al*. 1997). However, the potential for coupled flutter needed further investigation for the SD section, which exhibited relatively large absolute values of A_1^* and H_3^* compared to the OG section (Matsumoto *et al*. 2008).

3. Critical-modes identification by complex eigenvalue analysis

3.1 Identification of modes contribute to flutter instabilty

The flutter instability of the prototype FSPB was examined using complex eigenvalue analysis (CEVA) (Miyata and Yamada 1990). CEVA accounted for aeroelastic couplings among the considered modes and identified the critical modes contributing to flutter instability. A 3-dimensional structural analysis of the entire bridge was carried out using the RM Bridge structural analysis program (Bentley 2020). The finite-element analysis utilized the cross-sectional properties of the OG bridge. Table 2 presents the natural frequencies and corresponding mode shapes.

CEVA was performed on the twenty natural modes summarized in Table 2, using the flutter derivatives presented in Fig. 3. The initial structural damping ratios

Table 3 Flutter wind speed for the SD according to the mode combinations in CEVA

Considered modes	Flutter wind speed (m/s)
No. 1 ~ 20	16.7
No. 1 ~ 14	16.7
No. 2 ~ 6	17.0
No. 2 and 6	17.0
No. 6	36.5

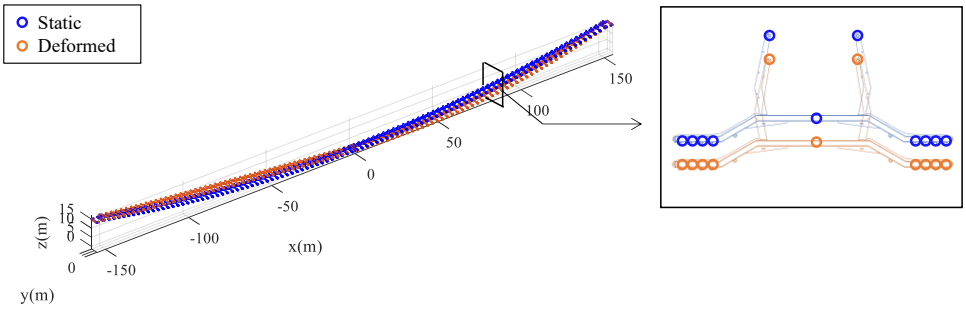

(a) V-A-1

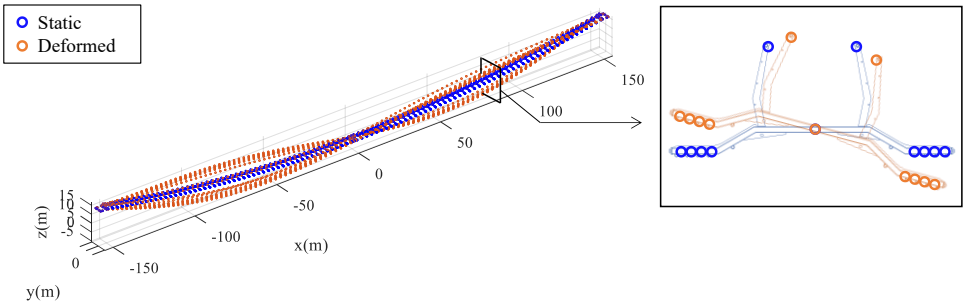

(b) T-A-1

Fig. 5 Mode shape of the prototype FSPB

were assumed to be 0.2% for all modes, according to the design guidelines (MOLIT 2021). The analysis produced changes in damping ratios, expressed as logarithmic decrements, with increasing wind speed for both OG and SD sections, as shown in Fig. 4. Fig. 4(a) demonstrates that the OG section remained safe from flutter-related issues, as all considered modes maintained positive total damping ratios even at the wind speed of 63.6 m/s. In contrast, Fig. 4 (b) indicates that several modes of the SD section developed negative damping ratios as the wind speed increased. The first zero-crossing of the damping ratio occurred at a wind speed of 16.7 m/s, initiated from the 1st anti-symmetric torsional mode (mode 6 in Table 2). This underscores the significant influence of the opening ratio of the deck grating on flutter instability in FSPBs.

To pinpoint the modes contributing to negative damping ratios, CEVA was repeated with various mode combinations, and the results are summarized in Table 3. When only mode 6 was considered, flutter instability was observed at 36.5 m/s, significantly higher than the flutter wind speed predicted with all modes included. This indicated that multiple modes contributed to flutter onset. A two-mode combination of modes 6 and 2 (the 1st anti-symmetric vertical mode) resulted in a flutter wind speed nearly identical to the twenty-mode case.

3.2 Contribution of lateral DOF

At this stage, the investigation into the flutter-developing mechanism of the FSPB focused solely on the SD section, as it had exhibited coupled flutter instability in CEVA. Fig. 5 shows the mode shapes of the 1st anti-symmetric vertical and torsional modes responsible for the coupled flutter, along with the deformed cross sections at the position of maximum displacement. The blue and orange dots represent the static state and the deformed shapes, respectively. Fig. 5 indicates that no pendulum-shaped or lateral motion was observed, even at the position of maximum deformation in both modes. Based on this observation, it was hypothesized that the lateral DOF would have a negligible influence on the coupled flutter onset of the FSPB. To check this hypothesis, additional CEVA was conducted with the lateral DOF omitted. The results were compared to analyses that include all DOF, focusing specifically on the 1st anti-symmetric vertical and torsional modes.

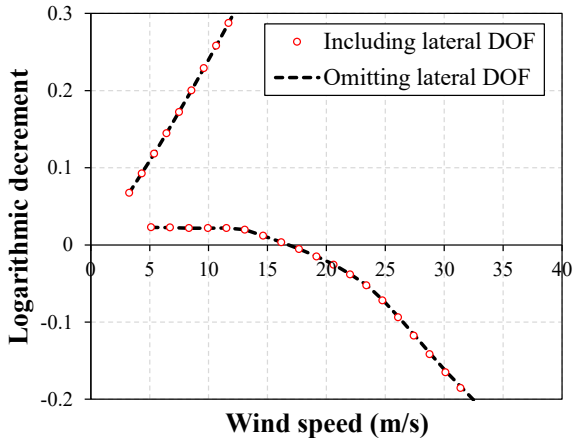

Fig. 6 Comparing the influence of lateral DOF on structural damping

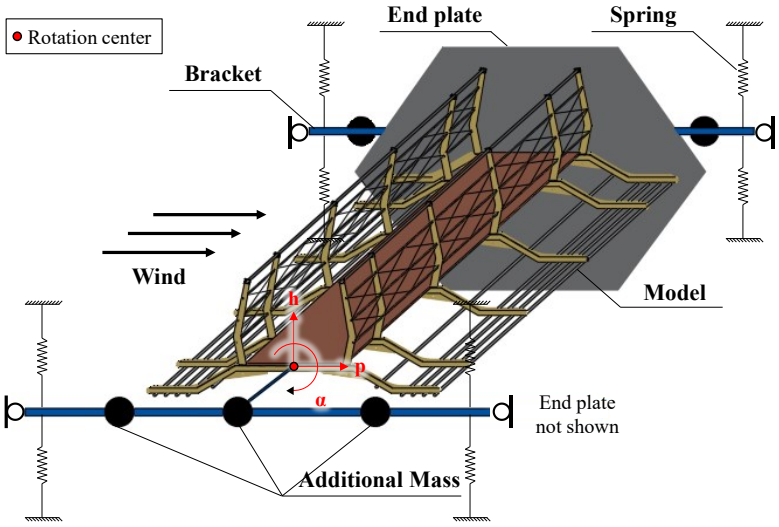

Fig. 7 Spring-supported system for vibration wind tunnel test

As shown in Fig. 6, constraining the lateral DOF for the two critical modes did not alter the flutter wind speed. It confirms that the coupling of the lowest vertical-torsional modes was the dominant mechanism in the coupled flutter of the prototype FSPB, and the influence of lateral modes and DOF was negligible. Consequently, the study concluded that conventional 2-D wind tunnel tests that are typically used to examine the flutter stability of road bridges are also applicable for evaluating the flutter stability of the FSPB.

4. Coupled flutter behavior and mechanism of FSPB

Based on the predicted flutter wind speed and the critical modes identified in Section 3, a series of 2-D wind tunnel tests were conducted to investigate the coupled flutter behavior. Although the wind tunnel test provides the most accurate observation of flutter behavior, it only measures displacement, making it challenging to fully understand the underlying force mechanisms. To address this issue, a two-DOF time-domain analysis was performed in parallel, offering deeper insights into the mechanism and key parameters driving the coupled flutter of FSPBs.

4.1 Experimental investigation on coupled flutter behavior

The experimental setup involved a section model elastically supported using four pairs of linear springs and brackets, designed to simulate both vertical and torsional DOFs. The spring-supported system is depicted in Fig. 7. The test setup targeted the 1st anti-symmetric vertical and torsional modes, with modal parameters determined based on the similitude law on a geometric scale length of 1:12, as detailed in Table 4.

End plates were attached on both sides of the model to secure the two-dimensional flow along the model by minimizing the end effects. Additional masses were located along the bracket to realize the target modal mass and the mass moment of inertia. The vertical and torsional displacements of the section model were measured using four laser displacement transducers located outside the wind tunnel. The sampling frequency of the displacement transducers was set to 500 Hz, with a sampling period of 60

Table 4 Similitude law and setup parameters for wind tunnel test

Parameter	Prototype	Model (target)	Model (measured)	Difference
Length, L (m)	10.8	0.9	0.9	0.00 %
Width, B (m)	4.450	0.371	0.371	0.00 %
Mass, m (kg/m)	524	3.640	3.642	0.06 %
Mass moment of inertia, I (kg·m^2/m)	1,027	0.050	0.048	-3.28 %
Vertical natural frequency, f_h (Hz)	0.283	1.885	1.885	0.00 %
Torsional natural frequency, f_α (Hz)	0.446	2.971	3.077	3.57 %
Frequency ratio, FR(= f_α/f_h)	1.576	1.576	1.633	3.57 %
Vertical damping ratio (%), $\xi_{h,struct}$	-	-	0.250	-
Torsional damping ratio (%), $\xi_{\alpha,struct}$	-	-	0.175	-

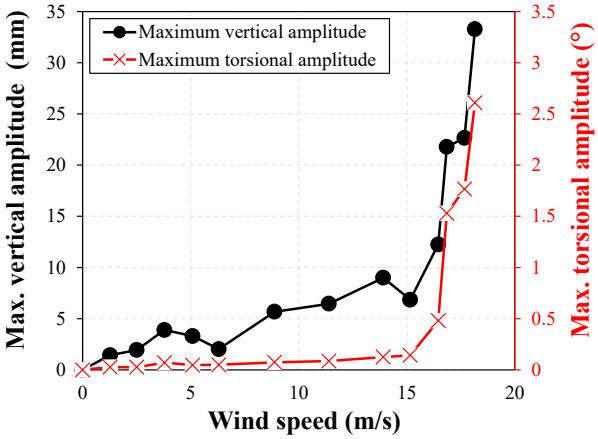

Fig. 8 Maximum vertical and torsional amplitudes

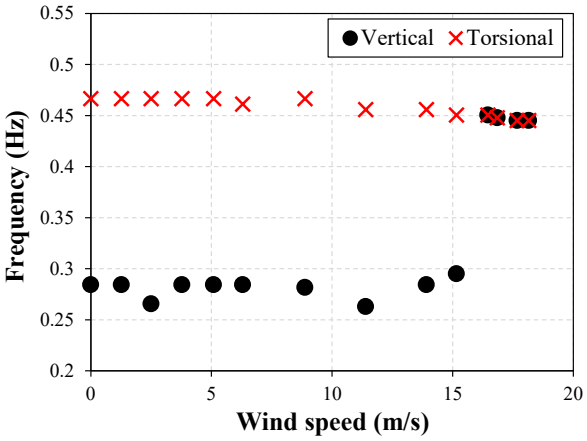

Fig. 9 Dominant motion frequencies for each DOF

seconds.

Fig. 8 shows the maximum displacements recorded during 60 seconds for each tested wind speed. Displacement and wind speed were converted to prototype scale. Flutter was defined as occurring when the torsional displacement exceeds 0.5°. The onset of flutter was identified at a wind speed of 16.4 m/s, where the torsional displacement sharply increased to more than 1°. The flutter wind speed aligns well with the prediction in Section 3. The dominant vibration frequencies for each DOF by wind speed were extracted from the response time histories by the fast Fourier transform (FFT) (Fig. 9). Notably, a pronounced frequency shift in the vertical motion, from its original frequency to the torsional frequency, demonstrated typical torsional mode-driven coupled flutter behavior, consistent with previous study (Abbas *et al*. 2017).

Two distinct frequency components, f_h, and f_α, were observed in the time histories of vertical displacement. Fig. 10 presents the vibration amplitudes of these components at each wind speed, obtained using a band-pass filter. In the post-flutter state (after the onset of flutter), the f_h component amplitude gradually diminished with increasing

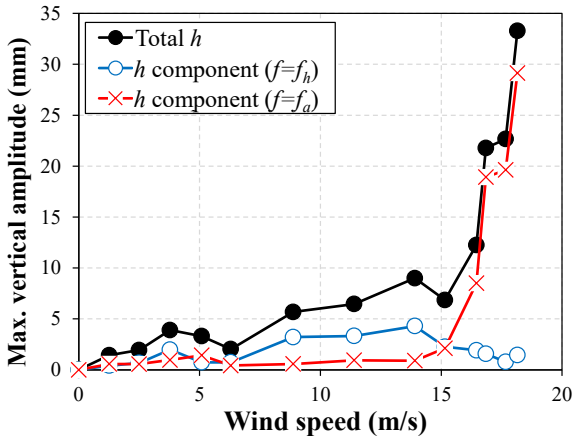

Fig. 10 Maximum vertical amplitude by the frequency component

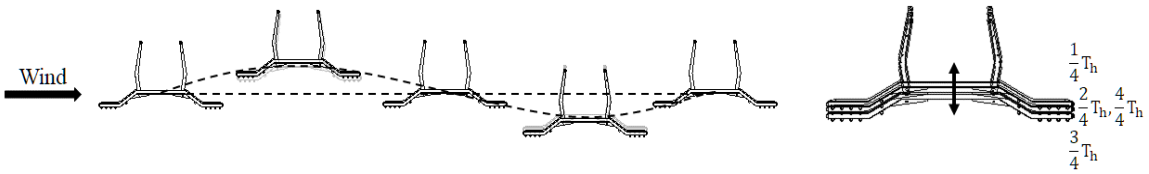

(a) before the onset of coupled flutter

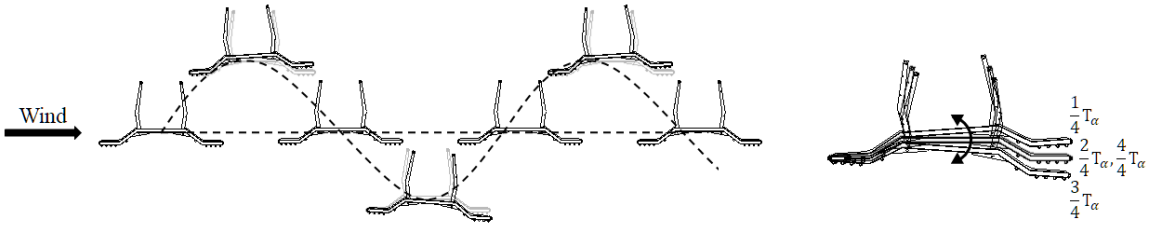

(b) post-flutter

Fig. 11 Vibration motion

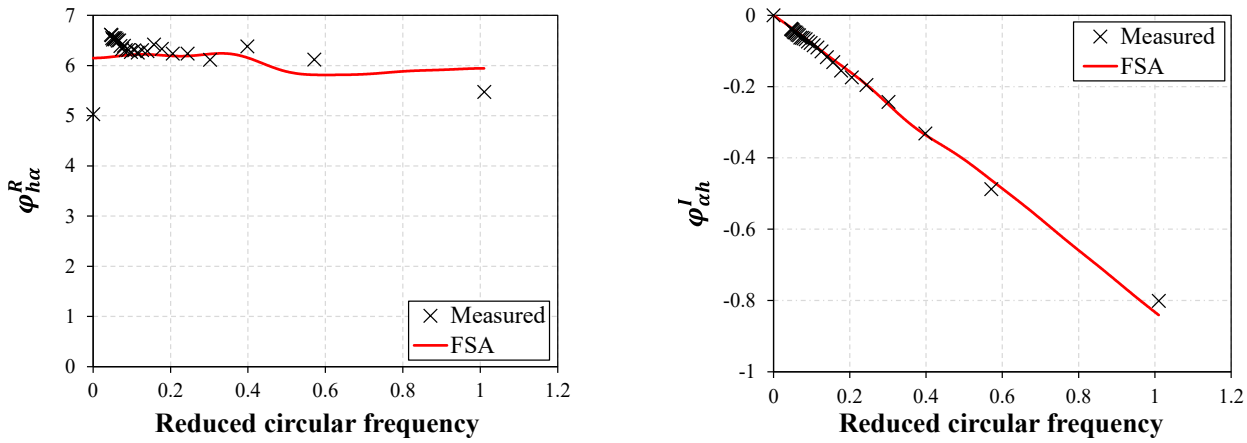

(a) $\varphi^R_{h\alpha}$ (b) $\varphi^I_{\alpha h}$

Fig. 12 Aerodynamic transfer function of SD

wind speed, attributed to enhanced aerodynamic damping of vertical motion. Conversely, the f_α component amplitude exhibited a rapid increase, highlighting the dominant influence of torsional motion in the post-flutter state.

Fig. 11 compares the movement of the section model before and after the onset of coupled flutter. In Fig. 11(a), the section model mainly exhibits vertical vibrations with a vertical natural period (T_h), showing minimal coupling effect and negligible torsional motion. After the onset of coupled flutter, as shown in Fig. 11(b), the f_α component dominated the vertical motion, causing vertical-torsional coupled oscillations. Both vertical and torsional motions

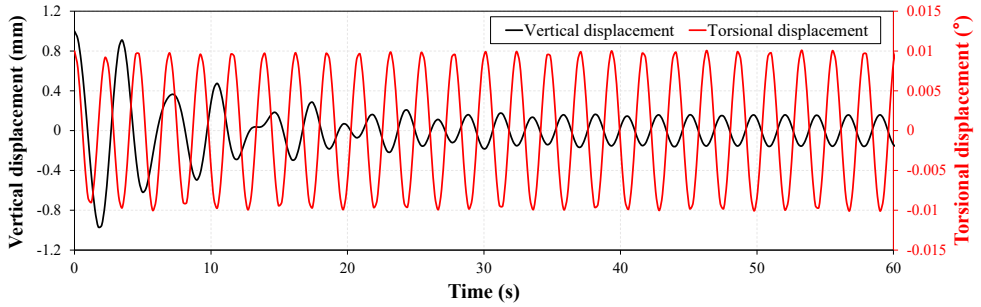

(a) displacements

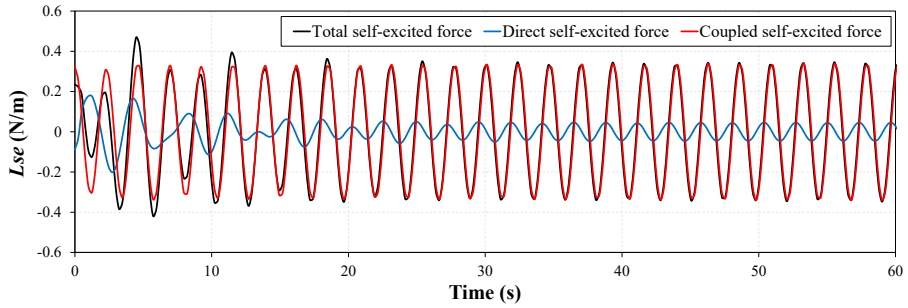

(b) L_{se}

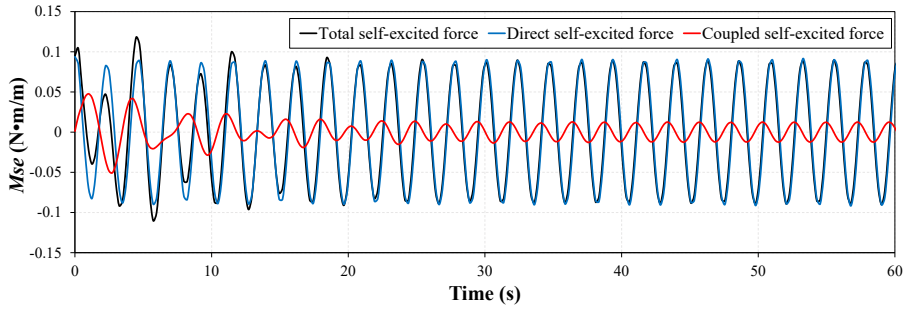

(c) M_{se}

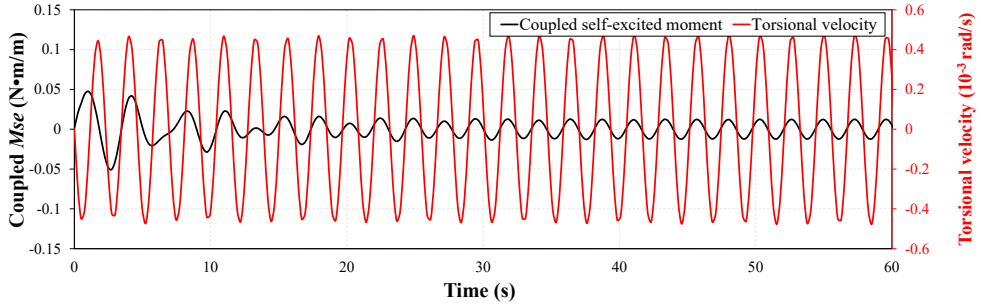

(d) phase synchronization of coupled M_{se} and $\dot{\alpha}$

Fig. 13 Time histories by FSA (U = 16.5 m/s)

occurred at the torsional natural period (T_α), shifting the rotational center windward compared with its position before the onset of coupled flutter. This shift in the rotational center is a distinct characteristic of the vibration pattern observed during coupled flutter.

4.2 Interpretation with a time-domain flutter analysis

The time-domain analysis employed the FSA method (Park *et al.* 2014). FSA utilizes the identical dynamic properties as summarized in Table 4, and the experimentally measured flutter derivatives (Fig. 3) to derive modified aerodynamic transfer functions, which are represented as trigonometric functions that satisfy the causality conditions. These modified transfer functions were subjected to an inverse Fourier transform to obtain the impulse response function. Subsequently, convolution integrals were applied to the time domain. Fig. 12 compares the aerodynamic transfer functions of the experimentally measured flutter derivatives with those approximated through the FSA method. This figure illustrates the real part of the aerodynamic transfer function ($\varphi_{h\alpha}^{R}$) in the h-direction and

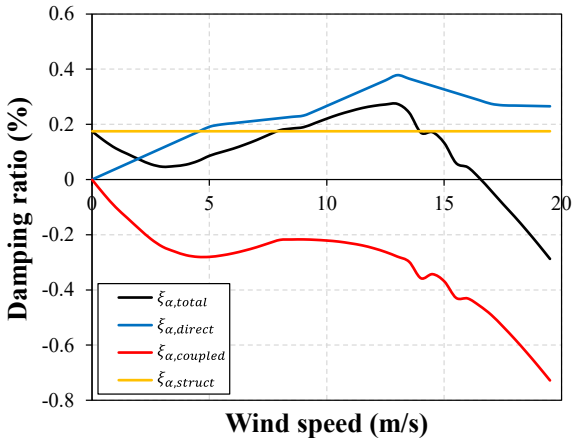

Fig. 14 Damping contributions in torsional DOF

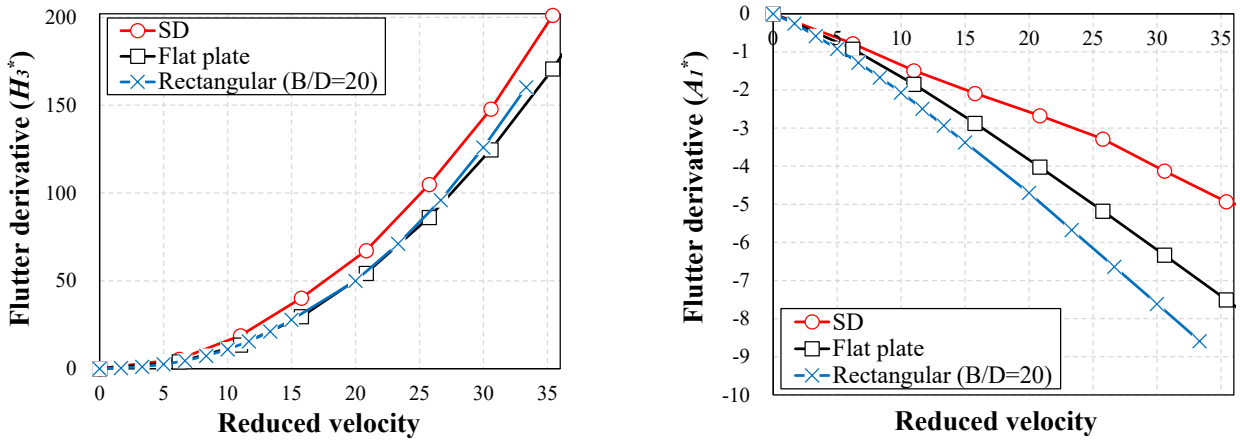

(a) H_3^* (b) A_1^*

Fig. 15 Comparisons of flutter derivatives

the imaginary part ($\varphi_{\alpha h}^I$) in the α-direction, which are associated with H_3^* and A_1^* known to have a significant impact on the coupled flutter, were close each other and the FSA was valid.

The initial displacements were set at 1 mm and 0.01° for vertical and torsional DOFs, respectively. Time-domain analysis predicted a coupled flutter occurrence at 16.5 m/s, which closely matched the experimentally observed flutter wind speed of 16.4 m/s. The alignment between the two methods implies that the experimentally observed flutter could be explained through time-domain analysis. Fig. 13 (a) presents the analyzed vertical and torsional vibration signals at the flutter wind speed. The vertical vibration of the f_h components gradually damped out during the initial 15 seconds, which was followed by a continuous generation of vertical vibration of the f_α component. The combination of vertical and torsional vibration signals, consistent with f_α and exhibiting a phase difference of 180°, explains the mechanism of post-flutter vibration motion shown in Fig. 11(b). Although the vertical and torsional modes each oscillate maintaining the original rotation center, their combination—at the same frequencies but opposite phases—gives the impression that the rotation center is shifted. Fig. 13(b) shows the separation of L_{se} into direct lift force related to vertical motion and coupled lift force related to torsional motion. It is observed that the coupled lift force dominates rather than the direct lift force, contributing significantly to L_{se}, amplifying the f_α component of vertical vibration, and causing a frequency shift. Fig. 13(c) shows the separation of M_{se} into direct moment related to torsional motion and coupled moment related to vertical motion. Notably, while the coupled moment is not the primary contributor to M_{se}, its phase aligns with $\dot{\alpha}$, as shown in Fig. 13(d). In the equation of motion of the torsional DOF, $\dot{\alpha}$ directly influences structural system damping. Thus, the coupled moment in phase with $\dot{\alpha}$ adversely impacts the damping of the torsional DOF.

To quantitatively evaluate the contribution of the coupled self-excited force to the damping of torsional DOF, additional analyses were conducted. The total damping ratio of the torsional DOF ($\xi_{\alpha,total}$) can be decomposed into the structural damping ratio ($\xi_{\alpha,struct}$), the aeroelastic damping from the direct self-excited moment ($\xi_{\alpha,direct}$), and that from the coupled self-excited moment ($\xi_{\alpha,coupled}$). In these analyses, $\xi_{\alpha,struct}$ corresponds to the torsional damping ratio, as defined in Table 4. $\xi_{\alpha,direct}$ and $\xi_{\alpha,coupled}$ are calculated based on the aeroelastic damping contributions from the $\dot{\alpha}$-dependent and $\dot{h}$-dependent

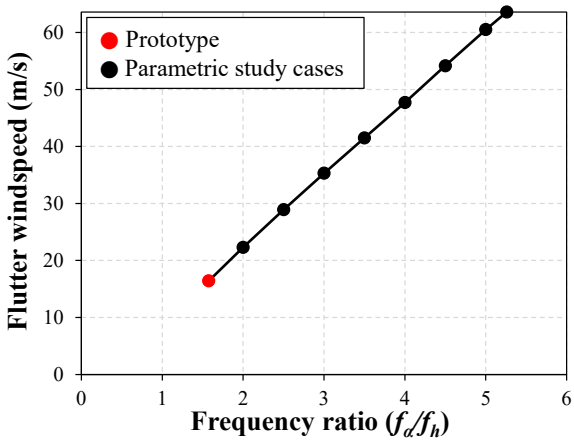

Fig. 16 Change of flutter wind speed with FR

terms in Eq. (2), respectively. Fig. 14 demonstrates how each component affects the total damping ratio at different wind speeds. As previously discussed, the damping effect caused by the coupled term acts as negative damping, decreasing the $\xi_{\alpha,total}$ and reaching zero at a wind speed of 16.5 m/s, at which point flutter occurs. This confirms the mechanism where torsional-induced vertical motion and its feedback in the coupled moment destabilize the structural system, ultimately causing a coupled flutter in the FSPB.

4.3 Discussions for the flutter instability at low wind speeds

As shown in Fig. 15, the coupled flutter derivatives H_3^* and A_1^* of the SD section exhibited trends similar to those of the flat plate (Amandolese *et al*. 2013) and the rectangular (B/D=20) cross-section (Matsumoto *et al*. 2010), both of which occurred coupled flutter at low wind speeds. Since the flutter derivatives of the SD section are similar to those of the flat plate and the rectangular (B/D=20) cross-sections, we anticipated coupled flutter under similar reduced velocities. However, due to the narrower deck width and the lower natural frequencies of FSPBs compared to road bridges, FSPBs with SD sections are prone to coupled flutter at relatively low wind speeds.

Moreover, the low FR between the lowest torsional and vertical mode frequencies could also contribute to coupled flutter instability. Long-span suspension road bridges are typically designed with an FR exceeding 2 to prevent coupled flutter (Gimsing and Georgakis 2011). For the studied FSPB, the FR of 1.58 is lower than that of long-span road bridges, facilitating easier aeroelastic force-coupling between vertical and torsional modes, which promotes coupled flutter instability.

To assess the influence of FR on flutter wind speed, repetitive time-domain analysis was conducted by varying only the torsional frequency while keeping other dynamic properties constant. As shown in Fig. 16, the flutter wind speed increased linearly with rising FR, confirming that a low FR enhances aeroelastic force-coupling between vertical and torsional modes, leading to coupled flutter instability at low wind speeds for FSPBs with an SD.

5. Conclusions

This study investigated the flutter instability of flexible suspended pedestrian bridges (FSPBs) with two types of deck designs. The open grating (OG) proved aerodynamically stable, whereas the solid deck (SD) exhibited coupled flutter at low wind speeds. The flutter behavior, developing mechanism, and governing parameters were identified for the SD.

- Aeroelastic analysis of the entire bridge, accounting for mode coupling in the SD, showed coupled flutter at a wind speed of 16.6 m/s caused by the 1st anti-symmetric torsional and vertical modes. Complex eigenvalue analysis (CEVA) case studies confirmed that the lateral modes and lateral degrees of freedom (DOF) made no contribution to the onset of coupled flutter and had negligible influence. These results validated the applicability of a two-DOF wind tunnel test setup for investigating the coupled flutter of FSPBs.
- For the 1st anti-symmetric torsional and vertical modes, 2-D wind tunnel tests revealed that at wind speed above 16.4 m/s, torsion-induced vertical displacement increased along with torsional displacement, resulting in coupled flutter. During coupled flutter, the frequencies of the two coupled modes coincided, accompanied by a shift in rotational center windward.
- The two-DOF time-domain flutter analysis shows that torsional displacement generates a coupled lift force, which induces vertical displacement at the torsional natural frequency. This vertical motion, in turn, generates additional coupled moment, creating a feedback loop. During this interaction, a 180° phase difference between the vertical velocity and torsional velocity emerges, causing the vertical motion to act as negative damping on the torsional system and leading to instability. The analysis confirms that force-damping feedback is a key mechanism in the development of coupled flutter.
- The couple flutter behavior of FSPBs at relatively low wind speeds arises from their unique aerodynamic and structural characteristics. Specifically, the flutter coefficients of SD section and the low frequency ratio (FR) between torsional and vertical frequencies significantly

amplify the coupling effects between these modes, leading to coupled flutter at low wind speeds.

Acknowledgments

This research is supported by the Korea Agency for Infrastructure Technology Advancement (KAIA) grant funded by the Ministry of Land, Infrastructure and Transport (Grant RS-2023-00250727) through the Korea Floating Infrastructure Research Center at Seoul National University.

References

Abbas, T., Kavrakov, I. and Morgenthal, G. (2017), "Methods for flutter stability analysis of long-span bridges: a review", *Proceedings of the Institution of Civil Engineers-Bridge Engineering*

Amandolese, X., Michelin, S. and Choquel, M. (2013), "Low speed flutter and limit cycle oscillations of a two-degree-of-freedom flat plate in a wind tunnel", *J. Fluid Struct*., **43**, 244-255. https://doi.org/10.1016 /j.jfluidstructs.2013.09.002.

Bentley (2020). *RM Bridge*. In Bentley Systems, incorporated.

Gimsing, N.J. and Georgakis, C.T. (2011), *Cable Supported Bridges: Concept and Design*, John Wiley & Sons.

Guan, Q., Liu, L., Gao, H., Wang, Y. and Li, J. (2022), "Research on soft flutter of 420m-span pedestrian suspension bridge and its aerodynamic measures", *Buildings*, **12**(8), 1173. https://doi.org/10.3390/buildings 12081173.

Jiménez-Alonso, J.F., Sáez, A., Caetano, E. and Magalhães, F. (2016), "Vertical crowd–structure interaction model to analyze the change of the modal properties of a footbridge", *J. Bridge Eng*., **21**(8), C4015004. https://doi.org/10.1061/(ASCE)BE.1943-5592.0000828.

Li, Y. and Li, C. (2020), "Experimental investigations on the flutter derivatives of the pedestrian-bridge section models", *KSCE J. Civ. Eng*., **24**(11), 3416-3434. https://doi.org/10.1007/s12205-020-0243-7.

Liu, W.Y., Tang, H.J., Yang, X. and Xie, J. (2020), "Improvement of dynamic responses of a pedestrian bridge by utilizing decorative wind chimes", *Wind Struct*, **30**(3), 317-323. https://doi.org/10.12989/was.2020.30.3.317.

Ma, R., Zhou, Q., and Li, M. (2020). "Effect of countermeasures on the galloping instability of a long-span suspension footbridge", *Wind Struct*, **30**(5), 499-509. https://doi.org/10.12989/was.2020.30.5.499

Matsumoto, M., Daito, Y., Yoshizumi, F., Ichikawa, Y. and Yabutani, T. (1997), "Torsional flutter of bluff bodies", *J. Wind Eng. Ind. Aerod*., **69**, 871-882. https://doi.org/10.1016/S0167-6105(97)00213-4.

Matsumoto, M., Matsumiya, H., Fujiwara, S. and Ito, Y. (2010), "New consideration on flutter properties based on step-by-step analysis", *J. Wind Eng. Ind. Aerod*., **98**(8-9), 429-437. https://doi.org/10.1016 /j.jweia.2010.02.001.

Matsumoto, M., Okubo, K., Ito, Y., Matsumiya, H. and Kim, G. (2008), "The complex branch characteristics of coupled flutter", *J. Wind Eng. Ind. Aerod*., **96**(10-11), 1843-1855. https://doi.org/10.1016/j.jweia. 2008.02.011.

Miyata, T. and Yamada, H. (1990), "Coupled flutter estimate of a suspension bridge", *J. Wind Eng. Ind. Aerod*., **33**(1-2), 341-348. https://doi.org/10.1016/0167-6105(90)90049-I.

MOLIT (2021), *Guideline for Suspended Footbridge Design*, Ministry of Land, Infrastructure, and Transport (MOLIT), Sejong-si, Republic of Korea.

Park, J., Jung, K., Hong, Y.H., Kim, H.K. and Lee, H.S. (2014), "Exact enforcement of the causality condition on the aerodynamic impulse response function using a truncated Fourier series", *J. Eng. Mech*., **140**(5). https://doi.org/10.1061/(ASCE)EM.1943-7889.0000721.

Rizzo, F., Caracoglia, L. and Montelpare, S. (2018), "Predicting the flutter speed of a pedestrian suspension bridge through examination of laboratory experimental errors", *Eng. Struct*., **172**, 589-613. https://doi.org/10.1016/j.engstruct.2018.06.042.

Sarkar, P.P., Jones, N.P. and Scanlan, R.H. (1994), "Identification of aeroelastic parameters of flexible bridges", *J. Eng. Mech*., **120**(8), 1718-1742. https://doi.org/10.1061/(ASCE)0733-9399(1994)120:8(1718).

Strømmen, E. (2010), *Theory of Bridge Aerodynamics*, Springer Science & Business Media.

Tadeu, A., da Silva, F.M., Ramezani, B., Romero, A., Škerget, L. and Bandeira, F. (2022), "Experimental and numerical evaluation of the wind load on the 516 Arouca pedestrian suspension bridge", *J. Wind Eng. Ind. Aerod*., **220**, 104837. https://doi.org/10.1016/j.jweia.2021.104837.

Tubino, F. (2018), "Probabilistic assessment of the dynamic interaction between multiple pedestrians and vertical vibrations of footbridges", *J. Sound Vib*., **417**, 80-96. https://doi.org/10.1016/j.jsv.2017.11.057.

Venuti, F., Racic, V. and Corbetta, A. (2016), "Modelling framework for dynamic interaction between multiple pedestrians and vertical vibrations of footbridges", *J. Sound Vib*., **379**, 245-263. https://doi.org/10.1016/ j.jsv.2016.05.047.

FR